


RESEARCH ARTICLE

Validation of an ultrahigh contrast divided subtracted inversion recovery technique using a standard T_1 phantom

Mark Bydder¹  | Fadil Ali² | Paul Condron^{1,3} | Daniel M. Cornfeld^{1,3} | Gil Newburn¹ | Eryn E. Kwon^{1,3,4} | Maryam Tayebi^{1,3} | Miriam Scadeng^{3,4} | Tracy R. Melzer^{5,6} | Samantha J. Holdsworth^{1,3} | Graeme M. Bydder^{1,7}

¹Mātai Medical Research Institute, Tairāwhiti-Gisborne, New Zealand

²Imaging Institute, Cleveland Clinic, Cleveland, Ohio, USA

³Department of Anatomy & Medical Imaging, Faculty of Medical and Health Sciences & Centre for Brain Research, University of Auckland, Auckland, New Zealand

⁴Auckland Bioengineering Institute, Auckland, New Zealand

⁵Department of Medicine, University of Otago, Christchurch, New Zealand

⁶New Zealand Brain Research Institute, Christchurch, New Zealand

⁷Department of Radiology, University of California San Diego, San Diego, California, USA

Correspondence

Mark Bydder, Mātai Medical Research Institute, Tairāwhiti-Gisborne, New Zealand.
Email: markbydder@gmail.com

Funding information

Friends of Mātai Blue Sky Fund; Wu Tsai Human Performance Alliance; Mangatawa Beale Williams Memorial Trust; JN & HB Williams Foundation; Mātai Ngā Māngai Māori; GE Healthcare; Kānoa Regional Economic Development & Investment Unit of New Zealand; Manaaki Moves Trust; Hugh Green Foundation; Fred Lewis Enterprise Foundation

Abstract

The divided subtracted inversion recovery (dSIR) is a high T_1 contrast technique that shows changes in white matter in patients with traumatic brain injury and hypoxic injury. The changes can be explained by small differences in T_1 ; however, to date, there has been no independent validation of the technique using a standard reference. The present study develops the theory of the dSIR signal and performs validation using the NIST/ISMRM T_1 phantom. Non-idealities are explored, including the influence of noise bias and finite repetition time (TR), which leads to the introduction of an optimally efficient TR for inversion recovery acquisitions. Results show excellent agreement with theoretical calculations.

1 | INTRODUCTION

A difference in T_1 between tissues is one of the primary mechanisms for generating contrast in magnetic resonance (MR) imaging. The idea is to acquire an image using parameter choices such that the physical evolution of the MR signal provides differentiation of (normal from abnormal) tissues based on the T_1 and/or other properties.¹ Several recent techniques have been developed for obtaining very high T_1 contrast from two

ABBREVIATIONS: C_{IR} , contrast (dM_{IR}/dT_1); CSF, cerebrospinal fluid; dSIR, divided Subtracted Inversion Recovery; E_{IR} , efficiency (M_{IR}/\sqrt{TR}); FLAWS-hc, fluid and water suppression-high contrast; IR, inversion recovery; mD, middle domain; M_{IR} , longitudinal magnetization; MP2RAGE, magnetization prepared 2 rapid acquisition gradient echo; MR, magnetic resonance; mTBI, mild traumatic brain injury; SNR, signal-to-noise ratio; TE, echo time; TI, inversion time; TR, repetition time.

inversion recovery (IR) images rather than a single image.²⁻⁷ They use simple mathematical operations—multiplication, addition, subtraction, and division—to generate image contrasts not attainable by conventional IR sequences.

Magnetization prepared 2 rapid acquisition gradient echo (MP2RAGE) is formed by dividing the product of the images by the sum of squares.² *FLuid And Water Suppression* (FLAWS) has three variants one of which (FLAWS-hc) is the difference divided by the sum.^{4,5} In both cases, any common factors between the acquisitions such as coil shading, proton density, and T_2 are normalized out to leave essentially a pure T_1 -weighted image. The weighting is modulated by a filter that can be used to suppress or emphasize T_1 s of interest. *Divided subtracted IR* (dSIR) is constructed similarly to FLAWS-hc, but without sign correction and using narrowly spaced inversion times (TIs) to bracket a T_1 of interest in the *middle Domain* (mD) (Figure 1—left). Writing the longitudinal magnetization (M_{IR}) as a function of short and long TIs (TI_1 and TI_2), the image is produced by Equation 1.

$$dSIR = \frac{M_{IR}(TI_2) - M_{IR}(TI_1)}{M_{IR}(TI_1) + M_{IR}(TI_2)} \quad (1)$$

The response of the dSIR signal has the shape of a bipolar filter (Figure 1 right) with high dynamic range in the mD and broad stopband outside the mD.

An example from a normal volunteer is shown in Figure 2 of IR source images and the dSIR image. The acquisition protocol (TI_1/TI_2 350/500) places the mD on white matter where it produces a high level of detail and a sharp delineation of the boundary between white matter and gray matter. Normal white matter appears as a generally low signal (dSIR <0) with some gray anatomical features (dSIR ~0). Recent studies have reported that abnormal white matter appears at the top of the dynamic range (dSIR ~1) in patients with hypoxic injury and mild traumatic brain injury (mTBI).⁸⁻¹¹

An example from a patient presenting with mTBI is shown in Figure 3.¹² The patient reported fatigue and attention difficulties at 21 h that were not present on follow-up at 64 h. The accompanying changes in white matter dSIR signal correspond to a T_1 difference of around 100 ms. This ability to visualize changes in T_1 is a feature of dSIR compared to conventional sequences that are less sensitive to T_1 .

Clinical findings such as these provide the motivation of the present study to quantify the dSIR signal, to validate the T_1 response, and to optimize the sensitivity of the sequence. The overall aim is to increase confidence in the results obtained in patients using dSIR and other 2-point IR techniques.

2 | METHODS

The study was conducted in accordance with the Declaration of Helsinki and approved by the Auckland Hospital Research Ethics Committee (approval number AHRECAH1006 in 2021). Informed consent was obtained from the subject whose images are used in this manuscript.

In vivo scans: IR fast spin echo (FSE), 3 T, echo train length 10, 32-channel head coil, bandwidth 260 Hz/pixel, 256×256 resolution, TR/TE 5000/12 ms, TIs 350 and 500 ms (parameters taken from previous works⁹). Inversion was achieved using the default adiabatic hyperbolic secant pulse (duration 10 ms). Images were generated on the scanner in DICOM format and taken offline for analysis.

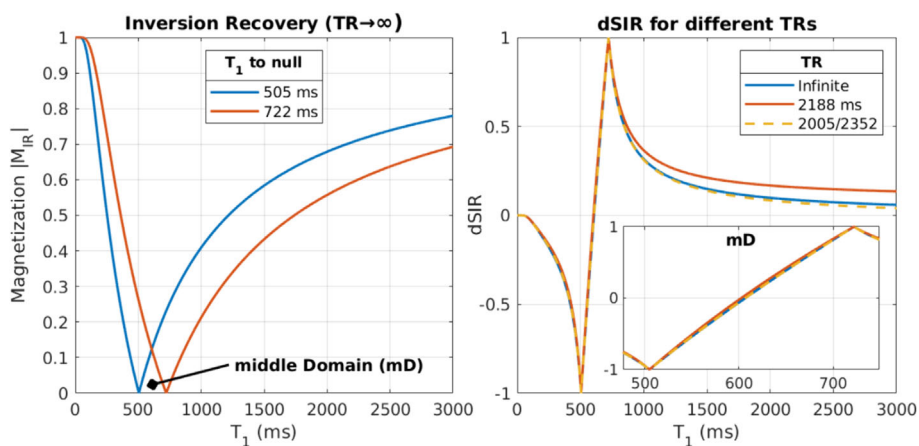


FIGURE 1 Magnetization as a function of T_1 for two inversion recovery (IR) curves (left) with nullpoints at 505 and 722 ms ($TI_1/TI_2 = 350/500$). The divided subtracted inversion recovery (dSIR) response (right) is linear between the nullpoints (inset) and damped outside resulting in a bipolar filter. The effect of repetition time (TR) is demonstrated for three TR choices (referred to later in the text) showing that differences are minimal inside the mD.

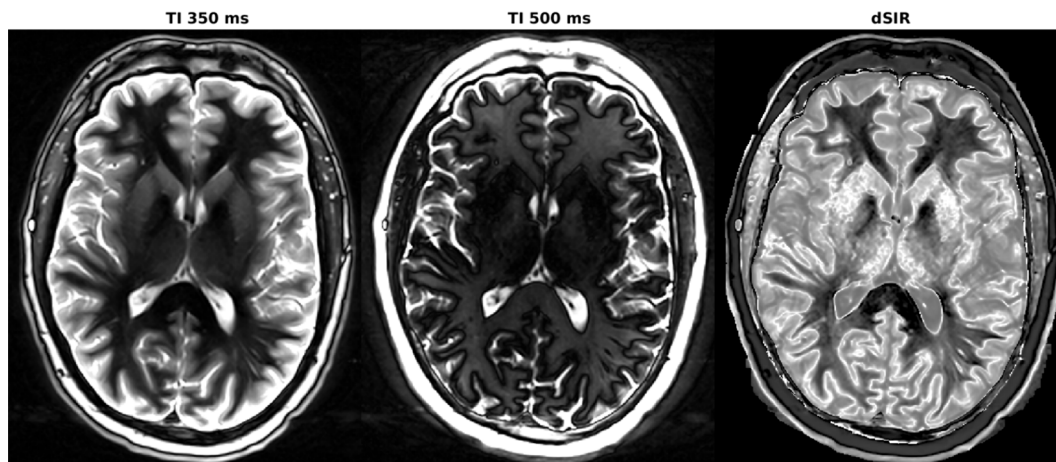


FIGURE 2 In vivo inversion recovery (IR) and divided subtracted inversion recovery (dSIR) images with $T_I = 350$ and 500 ms as well as the corresponding dSIR image. The source images show low signal in white matter and high signal in CSF. The dSIR (Equation 1) acts as a bipolar T_1 filter that suppresses unwanted short and long T_1 signals and generates high contrast inside the mD.

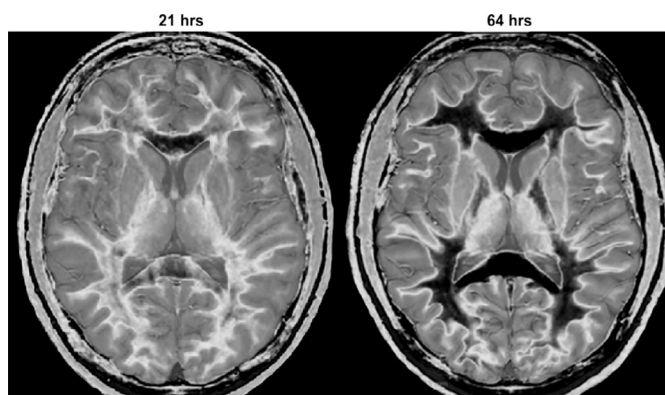


FIGURE 3 Divided subtracted inversion recovery (dSIR) images at 21 h (left) and 64 h (right) following an mTBI. High signal is observed in the white matter of the cerebral hemispheres shortly after injury (left). On the follow-up image (right), the white matter signal appears dark.

Phantom scans: IR spin echo (SE), 1.5 T, 2-channel body coil, bandwidth 1000 Hz/pixel, 128×128 resolution, TR/TE 15000/10 ms, T_I in increments of 100 ms from 24 to 1024 ms. Raw data were taken offline for analysis. Matched filter coil combination was used with a kernel size of 200 points.¹³ No other filtering or post-processing was applied.

Phantom: The phantom is commercially available as the NIST/ISMRM Premium System Phantom Model 130 (Caliber MRI, Boulder CO).¹⁴ It contains 14 $MnCl_2$ -doped compartments with reference T_1 values logarithmically spaced from 83.33 to 2376 ms (given in Table S2 of previous works¹⁴).

Computation: All computations were done using MATLAB 2023a (Mathworks, Natick MA) on a 16-core Xeon processor (Intel, Santa Clara CA). The dSIR images were created from Equation 1 using pairs of T_I s. Fitting of T_1 was performed using an in-house implementation of the damped Gauss-Newton algorithm to minimize the least squares error between Equation 2 and the (complex) data points with respect to a (complex) scaling parameter and (real) T_1 .

3 | RESULTS

3.1 | Relation to T_1

The IR magnetization is a function of T_I , T_1 and TR given by Equation 2.

$$M_{IR} = 1 - 2\exp(-T_I/T_1) + \exp(-TR/T_1) \quad (2)$$

Substituting Equation 2 into Equation 1 results in a complicated expression that cannot easily be simplified using Taylor expansions since the exponents are not small. However, simulations reveal that dSIR has a near-linear dependence on T_1 inside the mD (Figure 1B inset), which may be approximated by Equation 3.

$$\text{dSIR} \approx m \cdot T_1 + c \quad (3)$$

Linear regression between the nullpoints yields slope $m = 2/\Delta\text{nullpoints}$ and intercept $c = -\Sigma\text{nullpoints}/\Delta\text{nullpoints}$, which can be rewritten as $m = \ln 4 / \Delta\text{TI}$ and $c = -\Sigma\text{TI}/\Delta\text{TI}$ at infinite TR.⁷ Outside the mD the shape is approximately the inverse of Equation 3, which reflects the suppression of short and long T_1 values. Overall the dSIR response is that of a bipolar T_1 filter.

3.2 | Initial T_1 measurement

Figure 4 shows images of the phantom containing 14 compartments with different T_1 s and a maximum signal-to-noise ratio (SNR) of around 20. This is a suggested value for clinical images,¹⁵ and so the phantom dataset represents a practical noise level. Best fit T_1 values ($\pm 95\%$ confidence intervals) in each compartment were 71.6 ± 1.4 , 101.7 ± 1.3 , 147.4 ± 1.3 , 208.0 ± 1.2 , 270.0 ± 1.5 , 409.2 ± 1.9 , 560.0 ± 2.0 , 743.9 ± 2.2 , 978.8 ± 2.4 , 1264.0 ± 3.5 , 1515.3 ± 5.7 , 1868.8 ± 8.1 , 2149.9 ± 11.0 , 2440.3 ± 13.3 ms. These are in excellent agreement with reference values (correlation 0.9994, slope 1.0079 ± 0.021 , intercept -12 ± 25 ms) and serve as a validation of the experimental setup.

3.3 | Noise bias

The dSIR images are formed from magnitude IR images, which contain noise bias.¹⁶ This can be a concern for dSIR since the signal at the nullpoints is mostly bias. Bias may be modeled as a quadrature term, $\text{signal} \rightarrow \sqrt{\text{signal}^2 + \text{bias}^2}$, proportional to the noise standard deviation ($\text{bias} = k\sigma$) with scaling factor k dependent on imaging choices. Specific examples include^{13,17,18}

- i. 1 channel, magnitude ($k = \sqrt{\pi/2}$)
- ii. N channels, sum of squares ($k \approx \sqrt{\pi/2} \cdot \sqrt{N}$)
- iii. N channels, matched filter, magnitude ($k = \sqrt{\pi/2}$)
- iv. N channels, matched filter, phase-corrected ($k = \sqrt{\pi/4}$)

Table 1 shows results from the regions of interest (ROIs) indicated in Figure 4 (red and blue circles) drawn on images reconstructed by each method. In the red ROI, the standard deviation is the same for all methods, and the multichannel methods all have the same mean. In the blue ROI, the values differ significantly between methods due to bias.

The effect of bias on the dSIR signal is demonstrated in Figure 4 (right). The experimental data and theoretical curves indicate a rounding of sharp boundaries at the edge of the mD (notably in phantom compartments 6 and 9) and consequently a loss of dynamic range. The dynamic range can be estimated at the nullpoint by substituting $M_{\text{IR}}(T_1) > \text{bias}$ and $M_{\text{IR}}(T_2) = \text{bias}$ into the dSIR formula (Equation 1) to obtain

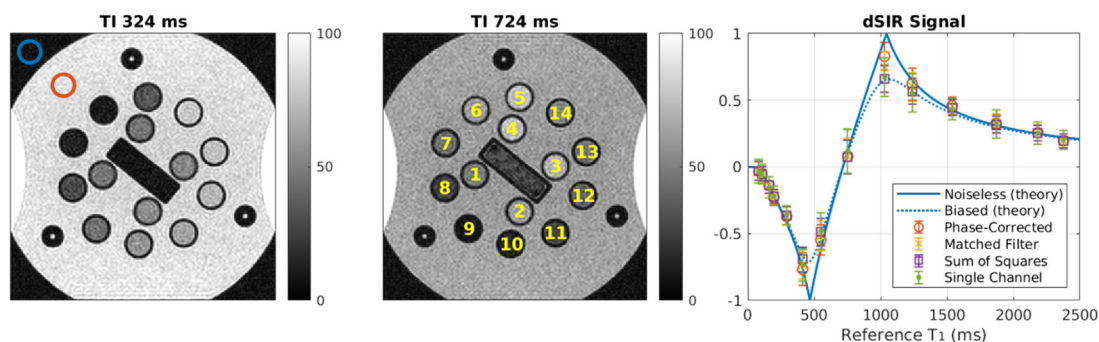


FIGURE 4 Phantom images with ROIs drawn in areas of containing bias (blue circle) and signal (red circle). The numbered compartments contain doped water with known T_1 s¹⁴. The plot (right) shows mean divided subtracted inversion recovery (dSIR) signal \pm standard deviation for each compartment using images generated by different reconstruction methods indicated in the legend. Overlaid are theoretical curves for the noiseless and noise-biased data.

$$\max.\text{dSIR signal} = \frac{\text{SNR} - k}{\text{SNR} + k} \quad (4)$$

where $\text{SNR} = M_{\text{IR}}(T_1)/\sigma$. Using phantom compartment 9 as representative of the nullpoint, the measured SNRs of 7.3 (single channel) and 9.6 (multichannel) yield estimates of the max. dSIR signal of 0.70, 0.69, 0.77, and 0.83 for methods (i)–(iv), respectively. These compare with the measured dSIR signals of 0.67, 0.66, 0.75, and 0.83. The results confirm the relative performance of methods (i)–(iv) and validate the effect of SNR on the dSIR signal given by Equation 4.

3.4 | T_1 ambiguity

A second consequence of using magnitude images is sign ambiguity in the dSIR. The phase difference ($\Delta\phi$) between the IR images can be used for disambiguation in a similar way to that used for FLAWS-hc.⁴ Briefly, $\Delta\phi$ is either $\pm\pi$ (inside the mD) or 0 (outside the mD); in the latter case, aliasing comes from the left (when $\text{dSIR} < 0$) or right (when $\text{dSIR} > 0$). Magnitude dSIR and sign-corrected dSIR images produced from following the disambiguation rules above are shown in Figure 5. The plot (right) shows how the latter resolves the full range of T_1 but exhibits noise sensitivity when dSIR is close to zero. This is expressed as misassigned pixels and a large standard deviation (notably phantom compartments 1–2). In comparison with the magnitude dSIR, however, two key features are lost: (i) long T_1 s appear at the top of the dynamic range, impairing the ability to visualize grayscale differences in the mD; (ii) boundaries at the edge of the mD at ± 1 are no longer present. These two qualitative aspects, namely, dynamic range reduction and boundary identification, are useful for clinically reading the images.

3.5 | Synthetic dSIR images

An important use for disambiguation is to allow remapping dSIR from one mD to another. This is possible because the signed dSIR has a one-to-one mapping with T_1 (and vice versa), so in principle any TI combination can be synthesized from any other. This idea was proposed previously for MP2RAGE to generate application-specific contrasts from a general-purpose wide ΔTI acquisition.¹⁹ The advantage is that precise TIs for an

TABLE 1 Values from the red/blue circular ROIs drawn on Figure 4 for different reconstruction methods. The standard deviation $\sigma \approx 4.7$ is consistent between methods, and the multichannel images have identical signal. The bias measurements differ depending on method, following the expected scaling (i)–(iv).

	Signal	Bias
Single channel	68.4 ± 4.6	5.7 ± 2.9
Sum of squares	89.0 ± 4.7	8.1 ± 3.0
Matched filter	88.8 ± 4.7	5.9 ± 3.2
Phase-corrected	88.7 ± 4.7	3.6 ± 2.7

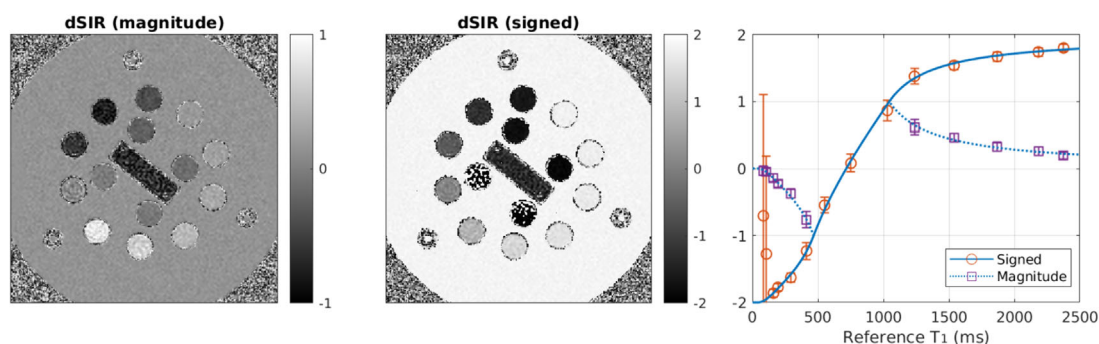


FIGURE 5 Divided subtracted inversion recovery (dSIR) image (left) for the phantom data in Figure 4 ($T_1/T_2 = 324/724$) and signed dSIR image (center) using the phase difference to disambiguate the signals. The plot (right) shows numeric values (\pm standard deviation) in each phantom compartment versus the reference T_1 values. Noise scatter in the short T_1 compartments reflects fluctuation in the dSIR signal from positive to negative about zero.

acquisition do not need to be known prospectively but can be synthesized in post-processing. A second application is to acquire slightly wider TIs than specified to move the nullpoints outside the mD (since these incur the most noise bias) then synthesize the required mD.

Examples of narrowing and widening ΔT_I are shown in Figure 6. The data points plotted versus the reference T_1 values accurately follow the theoretical curves. There is clearly some noise suppression/amplification associated with remapping, indicating some transforms are more favorable than others; however, a detailed analysis is beyond the scope of the present study.

3.6 | Efficiency

A long TR is frequently used for dSIR and MP2RAGE acquisitions. Reducing the TR allows the acquisitions to be performed in a shorter time but perturbs the shape of the T_1 response (Figure 7A). However, as long as the nullpoints are maintained by appropriate modification of the TIs by Equation 5

$$TI = T_1(\ln 2 - \ln(1 + \exp(-TR/T_1))) \quad (5)$$

then the filter shape is largely unchanged (Figure 1B). While the equilibrium magnetization is lower due to incomplete T_1 recovery, the acquisitions are faster, and so the efficiency as defined in Equation 6 is higher.

$$E_{IR} = \frac{M_{IR}}{\sqrt{TR}} \quad (6)$$

This reflects the fact that waiting for M_{IR} to recover yields diminishing returns and eventually saturates, whereas averaging always gives a square root increase in SNR with time. Figure 7B shows that E_{IR} passes through a maximum, which is the TR of optimal efficiency (TR_{opt}), and that TR_{opt} depends on the T_1 of interest. TR_{opt} also depends on the T_1 to null; Figure 7C plots TR_{opt} for some practical cases corresponding to the nulling of CSF, blood, and fat.

Table 2 compares three dSIR protocols based on the long TR protocol of previous works⁹ and two shorter TR protocols using either a fixed TR_{opt} or separate TR_{opt} s for each TI. The latter are optimized for a T_1 of interest at the center of the mD (613 ms), as described in Appendix B. Calculations show the theoretical efficiency gain using the shorter TR protocols is approximately 28%. To verify this, numerical simulations were performed using nonlinear least squares and dSIR (Equation 1) to estimate T_1 . Signals were generated from Equation 2 based on the protocols in Table 2 with added complex random Gaussian noise; the variance of the noise was scaled by the sum of the TRs to normalize for acquisition time. Means and standard deviations of the T_1 estimates were computed from 10^5 trials.

Figure 8 shows the standard deviations of T_1 s estimated by nonlinear least squares (solid lines) and dSIR (dashed lines). For both, the variation inside the mD has a similar shape with a minimum close to the center of the mD and minor differences at the edge of the mD. Differences outside the mD are due to the filtering effect of dSIR. Variation between the protocols is identical for least squares and dSIR, with coefficients of variation 1.000, 1.275, 1.276, respectively, at the T_1 of interest, consistent with the expected theoretical efficiency gain (Table 2). It should also be noted that the T_1 response between the protocols is almost identical in the mD (Figure 1B inset) outside the mD, there are differences at long T_1 signals due to the effect of short TR on the equilibrium magnetization. For the separate TR protocol, this causes the acquisitions to have more similar signal at long T_1 and thus better cancellation in the subtraction.

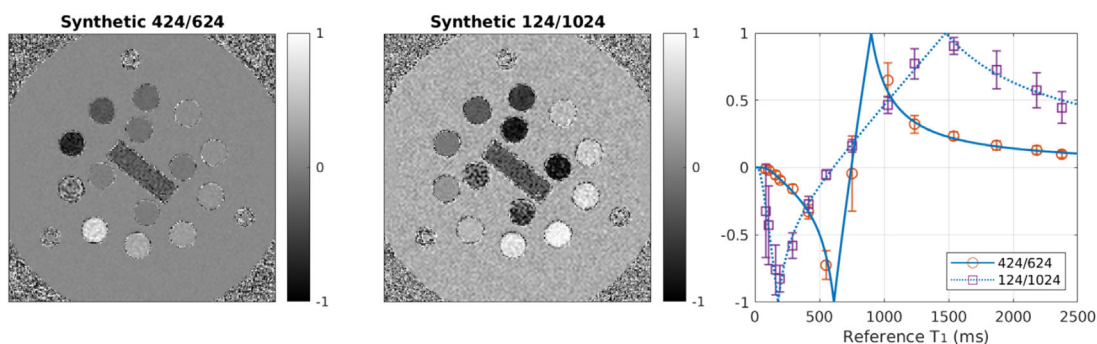


FIGURE 6 Examples of synthesizing divided subtracted inversion recoveries (dSIRs) to different inversion times (TIs) based on the dataset from Figures 4 to 5 ($TI_1/TI_2 = 324/724$). The left image shows narrowing to 424/624 and the center image shows widening to 124/1024. The plot (right) shows the signal (\pm standard deviation) in the different compartments overlaid with theoretical dSIR curves. Agreement between the remapped data and the expected filter shape is very close.

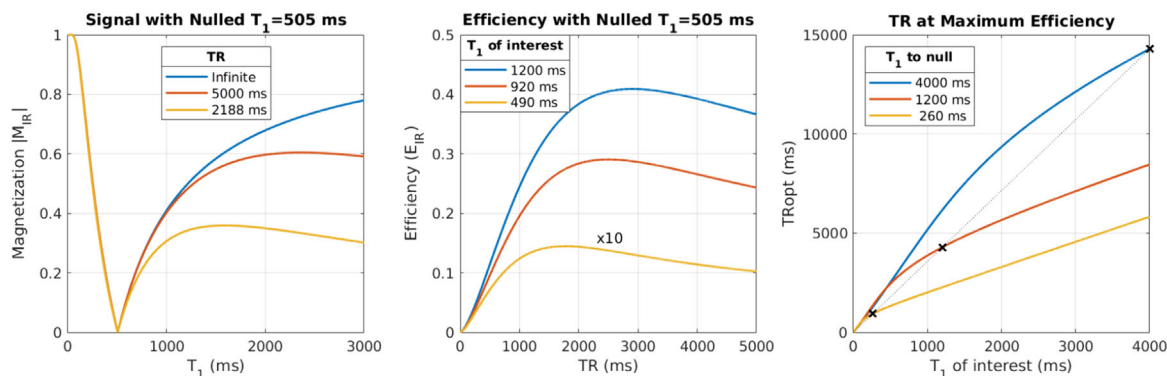


FIGURE 7 (A) Inversion recovery (IR) signal for different choices of repetition time (TR) with a nullpoint at $T_1 = 505$ ms. The longer T_1 signals are suppressed by use of a shorter TR, but signals in the mD are relatively unchanged. (B) Efficiency as a function of TR for different T_1 s of interest (scale is normalized to the SE sequence—see Appendix A). The efficiency is a strong function of TI particularly around the nullpoint (as may be expected). (C) The TR_{opt} versus T_1 of interest for some commonly nulled tissues: CSF (4000 ms), blood (1200 ms), and fat (260 ms). The black dotted line is the intersection of the T_1 of interest and T_1 to null at $TR = 3.57 T_1$ (see Appendix B).

TABLE 2 Repetition time (TR) and inversion time (TI) combinations that produce the same divided subtracted inversion recovery (dSIR) image. The shorter TRs have lower signal due to incomplete T_1 recovery but are more efficient (final column). The top two rows use a fixed TR for both TIs, while the bottom row uses a separate TR for each TI.

TR (ms)	T_{I1} (ms)	T_{I2} (ms)	M_{IR}	E_{IR}
5000	350	500	1.000 ^a	1.000 ^a
2188	343	466	0.848	1.282
2005/2352	341	473	0.842	1.286

^aCalculated at the center of the mD ($T_1 = 613$ ms) and normalized to the top row.

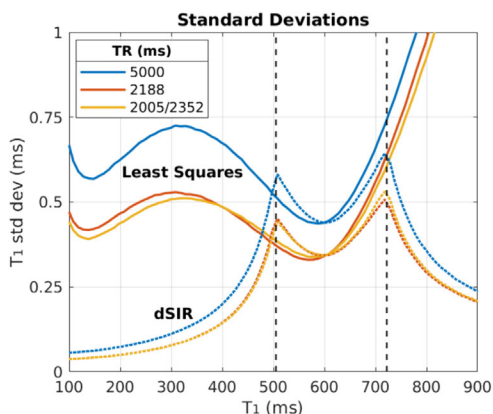


FIGURE 8 Numerical simulations of the standard deviation of T_1 estimated by nonlinear least squares (solid lines) and divided subtracted inversion recovery (dSIR) (dotted lines) based on the protocols in Table 2. Vertical dashed lines indicate the boundaries of the mD. Least squares and dSIR have similar shaped curves and minima in the mD, with differences outside the mD reflecting dSIR filtering (Figure 1). Comparing between protocols, the short TR protocols (red/yellow) generally exhibit around 28% lower uncertainty than the long TR protocol (blue), following the expected efficiency gain.

4 | DISCUSSION

Recent studies using the dSIR technique have described signal changes in patients with mTBI, multiple sclerosis and other diffuse brain disorders that are attributed to small changes in T_1 .^{8–12} The 2-point IR techniques such as dSIR, MP2RAGE, and FLAWS offer a hybrid qualitative–quantitative approach that filter unwanted T_1 signals yet retain a direct mapping to T_1 in physical units rather than arbitrary signal. This provides the motivation for the present study to improve understanding of the dSIR and optimize its sensitivity. Excellent agreement is observed between the theoretical model developed from Equations 1 and 2 and reference T_1 values in a standard phantom.

TABLE 3 Imaging protocols for inversion recovery (IR) sequences with TR_{opt} calculated based on literature T_1 s for CSF (4000 ms), fat (260 ms), brain (920 ms), and muscle (870 ms).²¹

Sequence	T_1 to null (ms)	T_1 of interest (ms)	TR_{opt} (ms)	Efficiency ^a	Contrast ^a
T_2 FLAIR	4000	920	4759	0.477	2.03
STIR	260	870	1837	0.543	0.30
T_1 FLAIR	4000	365 ^b	2000	0.549	1.52

^aCalculated relative to SE (Appendix A).

^bInferred from T_1 to null and the fixed repetition time (TR).

Previous work used a long TR which simplifies the signal model (Equation 2) but is suboptimal in terms of efficiency. A more time-efficient form of MP2RAGE with shortened TR and TIs was proposed using synthetic remapping to recover the T_1 response of a long TR acquisition,²⁰ however it is unclear how parameter values were chosen. The present study has found TR and TI can be specified by an optimization of the efficiency, which depends on the T_1 of interest and the T_1 to null. The approach generalizes to multi-TI acquisitions (corresponding to a vertical traversal of Figure 7C) and also single TI acquisitions. Examples of the latter are listed in Table 3. The TR_{opt} s predicted for T_2 FLAIR and STIR are close to the values used clinically, which indicates these sequences are optimized for efficiency (for comparison, optimization for contrast would use TRs of 3443 ms and infinity, respectively). The T_1 FLAIR sequence is designed maximize contrast between several tissues: fatty marrow ($T_1 = 260$ ms), white/gray matter ($T_1 = 790/920$ ms), and lesions ($T_1 = 1300$ ms). Its theoretical maximum efficiency (at 365 ms) and maximum contrast (at 619 ms) are intermediate between the target tissues.

The present study has several limitations. Firstly, the interpretation of dSIR as a surrogate for T_1 relies on the applicability of Equation 2, which is valid in water-based phantoms. However, biological tissues can have a range of complex behaviors. These include multiexponential relaxation and magnetization transfer effects,^{22–24} as well as technical differences due to the imaging sequence.²⁵ Secondly, experiments were performed using SE, whereas in practice, FSE is more common. Long echo trains of 180° RF pulses inhibit the recovery of longitudinal magnetization and require modification of the signal equation (i.e., replacing TR with $TR - TE_{last}$ where TE_{last} is the timing of the last echo).²¹ Another common sequence enhancement is driven equilibrium, which converts residual transverse magnetization at the end of the echo train to longitudinal magnetization.²⁶ Calculations of the optimal TI and TR with these techniques need to be modified. Thirdly, subtraction of images increases the sensitivity to noise. The SNR poses a fundamental limitation however noise bias is an avoidable second-order effect that causes a loss of dynamic range (Equation 4). A practical way to activate the optimal reconstruction pathway is to use matched filtering (parallel imaging or adaptive coil combine) with partial Fourier (phase constraints). Another option is to fit the T_1 using least squares and apply the dSIR filter retroactively. Noise suppression techniques, such as regularization and denoising, may also be useful at low SNR.

In conclusion, the dSIR sequence is a 2-point IR technique that provides high contrast and accurate T_1 estimates in a specific domain of interest. Good agreement is observed between theory and experiment, with expected systematic deviation due to the effect of noise bias at low SNR. These results help to increase confidence in clinical observations using the technique.

ACKNOWLEDGMENTS

This research was funded by the Fred Lewis Enterprise Foundation, the Hugh Green Foundation, Manaaki Moves Trust, the JN & HB Williams Foundation, the Mangatawa Beale Williams Memorial Trust, Anonymous Donor, an Agility Grant from the Wu Tsai Human Performance Alliance, Friends of Mātai Blue Sky Fund, and Kānoa—Regional Economic Development & Investment Unit of New Zealand. We are also grateful for support from GE Healthcare and Mātai Ngā Māngai Māori.

DATA AVAILABILITY STATEMENT

The data that support the findings of this study are available from the corresponding author upon reasonable request.

ORCID

Mark Bydder  <https://orcid.org/0000-0001-9210-0225>

ENDNOTE

* The precise factor is given by Eq 14 of Gudbjartsson and Patz¹⁶ however it is well-approximated by $1.1\sqrt{N}$ or simply just \sqrt{N} to illustrate the dependence on number of channels.

REFERENCES

- Young IR, Szeverenyi NM, Du J, Bydder GM. Pulse sequences as tissue property filters (TP-filters): a way of understanding the signal, contrast and weighting of magnetic resonance images. *Quant Imaging Med Surg*. 2020;10(5):1080-1120. doi:10.21037/qims.2020.04.07
- Marques JP, Kober T, Krueger G, van der Zwaag W, Van de Moortele PF, Gruetter R. MP2RAGE, a self bias-field corrected sequence for improved segmentation and T₁-mapping at high field. *Neuroimage*. 2010;49(2):1271-1281. doi:10.1016/j.neuroimage.2009.10.002
- Tanner M, Gambarota G, Kober T, et al. Fluid and white matter suppression with the MP2RAGE sequence. *J Magn Reson Imaging*. 2012;35(5):1063-1070. doi:10.1002/jmri.23532
- Beaumont J, Saint-Jalmes H, Acosta O, et al. Multi T₁-weighted contrast MRI with fluid and white matter suppression at 1.5 T. *Magn Reson Imaging*. 2019;63:217-225. doi:10.1016/j.mri.2019.08.010
- Beaumont J, Gambarota G, Saint-Jalmes H, et al. High-resolution multi-T₁-weighted contrast and T₁ mapping with low B1+ sensitivity using the fluid and white matter suppression (FLAWS) sequence at 7T. *Magn Reson Med*. 2021;85(3):1364-1378. doi:10.1002/mrm.28517
- Dokumacı AS, Aitken FR, Sedlacik J, et al. Simultaneous optimization of MP2RAGE T₁-weighted (UNI) and FLuid and white matter suppression (FLAWS) brain images at 7T using extended phase graph (EPG) simulations. *Magn Reson Med*. 2023;89(3):937-950. doi:10.1002/mrm.29479
- Ma YJ, Moazamian D, Cornfeld DM, et al. Improving the understanding and performance of clinical MRI using tissue property filters and the central contrast theorem, MASDIR pulse sequences and synergistic contrast MRI. *Quant Imaging Med Surg*. 2022;12(9):4658-4690. doi:10.21037/qims-22-394
- Newburn G, McGeown JP, Kwon EE, et al. Targeted MRI (tMRI) of small increases in the T₁ of normal appearing white matter in mild traumatic brain injury (mTBI) using a divided subtracted inversion recovery (dSIR) sequence. *OBM. Neurobiology*. 2023;7(4):1-27. doi:10.21926/obm.neurobiol.2304201
- Cornfeld D, Condrón P, Newburn G, et al. Ultra-high contrast MRI: using divided subtracted inversion recovery and divided echo subtraction sequences to study the brain and musculoskeletal system. *Bioengineering*. 2024;11(5):441. doi:10.3390/bioengineering11050441
- Newburn G, Condrón P, Kwon EE, et al. Diagnosis of delayed post-hypoxic leukoencephalopathy (Grinker's myelinopathy) with MRI using divided subtracted inversion recovery sequences: time for reappraisal of the syndrome? *Diagnostics*. 2024;14(4):418. doi:10.3390/diagnostics14040418
- Losa L, Peruzzo D, Galbiati S, Locatelli F, Agarwal N. Enhancing T₁ signal of normal-appearing white matter with divided subtracted inversion recovery: a pilot study in mild traumatic brain injury. *NMR Biomed*. 2024;37(10):e5175. doi:10.1002/nbm.5175
- Condrón P, Cornfeld DM, Scadeng M, et al. Ultra-high contrast MRI: the whiteout sign shown with divided subtracted inversion recovery sequences in post-insult leukoencephalopathy syndromes (PILS). *Tomography*. 2024;10(7):983-1013. doi:10.3390/tomography10070074
- Walsh DO, Gmitro AF, Marcellin MW. Adaptive reconstruction of phased array MR imagery. *Magn Reson Med*. 2000;43(5):682-690. doi:10.1002/(SICI)1522-2594(200005)43:5<3.0.CO;2-G
- Stupic KF, Ainslie M, Boss MA, et al. A standard system phantom for magnetic resonance imaging. *Magn Reson Med*. 2021;86(3):1194-1211. doi:10.1002/mrm.28779
- Owen RS, Wehrli FW. Predictability of SNR and reader preference in clinical MR imaging. *Magn Reson Imaging*. 1990;8(6):737-745. doi:10.1016/0730-725X(90)90009-Q
- Gudbjartsson H, Patz S. The Rician distribution of noisy MRI data. *Magn Reson Med*. 1995;34(6):910-914. doi:10.1002/mrm.1910340618
- Dietrich O, Raya JG, Reeder SB, Ingrisch M, Reiser MF, Schoenberg SO. Influence of multichannel combination, parallel imaging and other reconstruction techniques on MRI noise characteristics. *Magn Reson Imaging*. 2008;26(6):754-762. doi:10.1016/j.mri.2008.02.001
- Bydder M, Larkman DJ, Hajnal JV. Combination of signals from array coils using image-based estimation of coil sensitivity profiles. *Magn Reson Med*. 2002;47(3):539-548. doi:10.1002/mrm.10092
- Massire A, Seiler C, Troalen T, et al. T₁-based synthetic magnetic resonance contrasts improve multiple sclerosis and focal epilepsy imaging at 7T. *Invest Radiol*. 2021;56(2):127-133. doi:10.1097/RLI.0000000000000718
- Bapst B, Massire A, Mauconduit F, et al. Pushing MP2RAGE boundaries: ultimate time-efficient parameterization combined with exhaustive T₁ synthetic contrasts. *Magn Reson Med*. 2024;91(4):1608-1624. doi:10.1002/mrm.29948
- Bernstein MA, King KF, Zhou XJ. *Handbook of MRI pulse sequences*. Elsevier Inc.; 2004:961.
- Rioux JA, Levesque IR, Rutt BK. Biexponential longitudinal relaxation in white matter: characterization and impact on T₁ mapping with IR-FSE and MP2RAGE. *Magn Reson Med*. 2016;75(6):2265-2277. doi:10.1002/mrm.25729
- Manning AP, MacKay AL, Michal CA. Understanding aqueous and non-aqueous proton T₁ relaxation in brain. *J Magn Reson*. 2021;323:106909. doi:10.1016/j.jmr.2020.106909
- Karampekios S, Papanikolaou N, Papadaki E, et al. Quantification of magnetization transfer rate and native T₁ relaxation time of the brain: correlation with magnetization transfer ratio measurements in patients with multiple sclerosis. *Neuroradiology*. 2005;47(3):189-196. doi:10.1007/s00234-005-1344-1
- Boudreau M, Karakuzu A, Cohen-Adad J, et al. Repeat it without me: crowdsourcing the T₁ mapping common ground via the ISMRM reproducibility challenge. *Magn Reson Med*. 2024;92(3):1115-1127. doi:10.1002/mrm.30111
- Bernstein MA, King KF, Zhou XJ. *Handbook of MRI pulse sequences*. Elsevier Inc.; 2004:890. doi:10.1016/B978-012092861-3/50021-2
- Boxerman JL, Rosen BR, Weisskoff RM. Signal-to-noise analysis of cerebral blood volume maps from dynamic NMR imaging studies. *J Magn Reson Imaging*. 1997;7(3):528-537. doi:10.1002/jmri.1880070313
- Kurtz D, Dwyer A. Isosignal contours and signal gradients as an aid to choosing MR imaging techniques. *J Comput Assist Tomogr*. 1984;8(5):819-828. doi:10.1097/00004728-198410000-00002

How to cite this article: Bydder M, Ali F, Condrón P, et al. Validation of an ultrahigh contrast divided subtracted inversion recovery technique using a standard T₁ phantom. *NMR in Biomedicine*. 2024;37(12):e5269. doi:10.1002/nbm.5269

APPENDIX A: Efficiency of IR relative to SE

Equation 6 expresses the efficiency in arbitrary units. A more meaningful metric comes from dividing E_{IR} by the noise standard deviation to give the SNR efficiency; however, an alternative is to reference to a sequence without an IR pulse. The SE signal is given by $M_{SE} = 1 - \exp(-TR/T_1)$, which has maximum efficiency ($E_{SE} = M_{SE}/\sqrt{TR}$) at $TR \approx 1.26T_1$,²⁷ leading to $E_{SE} \approx 0.64/\sqrt{T_1}$. Using this normalization shows that E_{IR} is typically is less than half E_{SE} (Figure 7B). As well as efficiency, the contrast ($C_{IR} = dM_{IR}/dT_1$) can also be referenced to SE. The maximum of $C_{SE} = dM_{SE}/dT_1$ occurs at $TR = 2T_1$ with value $2\exp(-2)/T_1$ in arbitrary units. The maximum of C_{IR} is intractable except for $TR \rightarrow \infty$ where it has a maximum of $4\exp(-2)/T_1$ at $TI = 2T_1$,²⁸ or $2C_{SE}$. Thus, it can be seen that IR is around half as efficient as SE but has twice the available contrast.

APPENDIX B: Calculating TR_{opt} with narrow ΔTI

When the ΔTI is narrow, the T_1 of interest and T_1 to null are similar. In the limit that they are the same, the TR_{opt} can be found analytically by setting $dE_{IR}/dTR = 0$ and substituting $TR = \kappa \cdot T_1$. This leads to $\kappa(1+2\kappa) - (1+2\kappa+e^\kappa)(\ln 2 - \ln(1+e^{-\kappa})) = 0$, or $\kappa \approx 3.57$. In general the T_1 s are not the same and a numerical procedure must be used to calculate TR_{opt} . MATLAB code is given below for a specified T_1 of interest (T_{1int}) and T_1 to null (T_{1null}).

```

%% code to optimize TR for a given T1 of interest & T1 to null
T1int = 920;
T1null = 4000;

% avoid the singularity at TR = 0
initial_guess = 3.57 * T1int;

% find the minimum of -efficiency
wrapper = @(TR) -efficiency (TR, T1int, T1null);
TRopt = fminsearch (wrapper, initial_guess);

% display results
[E T I M C] = efficiency (TRopt, T1int, T1null);
fprintf ('TRopt = %f TI = %f M = %f E = %f C = %f\n', TRopt, TI, M, E, C);

%% function to calculate efficiency & contrast
function [E T I M C] = efficiency (TR, T1int, T1null)

% TI needed for T1null
TI = T1null * (log(2) - log(1 + exp[-TR/T1null]));

% magnetization at T1int
M = 1 - 2*exp(-TI/T1int) + exp(-TR/T1int);

% efficiency at T1int (relative to spin echo)
E = abs(M) / TR^(1/2);
E = E / (0.64/T1int^(1/2));

% contrast at T1int (relative to spin echo)
C = abs(exp(-TR/T1int)*TR - 2*exp(-TI/T1int)*TI) / T1int^2;
C = C / (2*exp(-2) / T1int);

end

```